

Ray-tracing laser-deposition model for plasma particle-in-cell simulation

A. Hyder*

*Dept. of Applied Physics and Applied Mathematics,
Columbia University, New York, NY 10027, USA*

W. Fox†

*Dept. of Astrophysical Sciences, Princeton University, Princeton, NJ 08544, USA and
Princeton Plasma Physics Laboratory, Princeton, NJ 08540, USA*

K. V. Lezhnin

Princeton Plasma Physics Laboratory, Princeton, NJ 08540, USA

S. R. Totorica

*Dept. of Astrophysical Sciences, Princeton University, Princeton, NJ 08544, USA and
Dept. of Astro-fusion Plasma Physics (AFP), Headquarters for Co-Creation Strategy,
National Institutes of Natural Sciences, Tokyo 105-0001, Japan*

(Dated: December 12, 2024)

We develop a ray-tracing model for laser-plasma interaction suitable for coupling in-line into kinetic particle-in-cell plasma simulation. The model is based on inverse Bremsstrahlung absorption and includes oblique incidence effects and reflection at the critical surface. The energy deposition is given to electrons by randomized kicks to momentum. The model is verified against analytic solutions and a 2-D laser ray-tracing code.

I. INTRODUCTION

Kinetic plasma simulations are a valuable tool for understanding high-energy-density (HED) plasma systems driven by intense radiation and energy sources [1]. Modern high-energy lasers, such as those at the National Ignition Facility (NIF) and OMEGA facility, couple several kJ of energy into \sim mm volumes of plasma within ns-timescales [2]. These lasers readily heat plasmas to keV temperatures, producing plasmas with long mean free paths. Furthermore, these plasmas can self-generate magnetic fields of 10's of Tesla sufficient to magnetize the plasma. Kinetic simulations can be valuable tools for understanding these systems, as they do not assume local Maxwellian distributions in the plasma. They can more readily handle kinetic effects, such as particle counter-streaming and temperature anisotropy, as well as simulate kinetic plasma processes, such as the formation of collisionless shocks [3–5], magnetic field generation by Weibel instability [6], and magnetic reconnection [7, 8]. To improve fidelity when designing and interpreting these experiments via simulations, a key step is to accurately simulate how the laser propagates and heats the plasma. For the laser pulses of interest in the present work, we consider how to model laser deposition via inverse Bremsstrahlung (IB), which is the collisional absorption of the laser photons by plasma.

In this paper, we develop a radiation transport model for laser propagation and absorption suitable for coupling

in-line into a kinetic plasma particle-in-cell simulation. The model traces laser intensity along rays using geometric optics, with laser absorption and energy deposition based on inverse Bremsstrahlung (IB) [9]. In this class of model, the laser-intensity envelope is simulated rather than the full-wave evolution of the electromagnetic (EM) fields. This relaxes the simulation requirements so that the laser wavelength and frequency do not have to be resolved by the simulation. This approach is often used in radiation hydrodynamics simulation (e.g., Refs. [10, 11]) and has been previously used in hybrid (kinetic ion) simulations [12]. This type of model has also been extended to incorporate full-wave effects near critical surfaces where the geometric optics break down [13].

We note that this approach differs from many full EM-wave simulations in laser-plasma interaction, which are most commonly used for direct simulation of laser-plasma instabilities and laser-driven particle acceleration (e.g., Ref. [14]). Models retaining the full EM-wave propagation must resolve the laser wavelength and frequency, which is computationally demanding, so that approach is usually limited to rapid phenomena and small-volume simulations. PIC models with full EM waves and Monte-Carlo collisions have been developed to study IB [15], though there are subtleties of the particle collisions during IB absorption [16, 17] which may not be captured in standard PIC Monte-Carlo collision routines [18]. At an even more fundamental description, IB has also been simulated with full-wave molecular dynamics simulation [19]. This type of model imposes the minimum amount of additional assumptions and, for example, directly resolves all particle collision processes, enabling prediction of transport factors such as the Coulomb logarithm. However, this method is the most computationally ex-

* a.hyder@columbia.edu

† wfox@pppl.gov

pensive and prohibitive for large-volume HED plasma simulations.

The model developed here follows the ray-tracing technique with IB absorption. The primary design choices were motivated by the goal of obtaining a fast, simple model that can be run in-line but with enough physics to compare to radiation-hydrodynamic simulations. This is to allow direct comparisons between a full kinetic treatment and radiation-hydrodynamic simulation of laser-heated plasmas. Rays are followed in 1-D (without refraction in the simulation domain) but with a technique that includes oblique incidence effects and ray reflection. The model is implemented in the Plasma Simulation Code (PSC) [20]. Two companion manuscripts [21, 22] present benchmarking of the laser deposition and plasma evolution with comparison to radiation-hydrodynamic simulations, thereby presenting additional dynamical verification of this model.

Section II reviews the theoretical model for calculating the power deposited by a laser when propagating through a plasma. The numerical implementation is presented in Section III. Additionally, the method for transferring the energy to the particles is described in Section III C. In Section IV, we present benchmarking against analytical ray-tracing solutions and another ray-tracing code, as well as benchmarking of the energy conservation. We briefly discuss some miscellaneous implementation notes of the algorithms in a parallel code in Section V, and we give our conclusions in Section VI.

II. LASER DEPOSITION MODEL

In this section, we recapitulate the laser propagation and inverse-Bremsstrahlung absorption in a plasma to present the model equations for ray-tracing and energy deposition.

For a laser propagating through a plasma, it is convenient to follow the laser intensity along rays rather than the full EM field evolution. This approach is valid when the laser wavelength is much shorter than other scales in the plasma. In this case, the laser propagation follows from geometric optics, which involves refraction and reflection when propagating through density gradient regions, and absorption. The spatial absorption of the laser energy due to collisions in the plasma is given by

$$P_{\text{abs}} = KI_s = -\frac{dI_s}{ds}, \quad (1)$$

where s indicates the spatial distance along the ray path. Here we use I_s as the laser intensity through a plane normal to s .

Following Dawson, *et al.* [9], the inverse-Bremsstrahlung absorption coefficient K for a plasma is

$$K = K_0 \frac{n_e^2}{n_{\text{cr}}} \frac{1}{(1 - n_e/n_{\text{cr}})^{1/2}}, \quad (2)$$

where K_0 is the absorption factor, n_e is the local electron density, and n_{cr} is the critical density [9]. At the critical density n_{cr} , the laser frequency $\omega = 2\pi f$ equals the local plasma frequency $\omega_{pe} = (4\pi n_e e^2/m_e)^{1/2}$. The absorption factor K_0 is

$$K_0 = \frac{4}{3} \left(\frac{2\pi}{m_e} \right)^{1/2} \frac{Z_{\text{eff}} e^4}{c (k_B T_e)^{3/2}} \ln \Lambda_{\text{IB}}, \quad (3)$$

Here m_e is the electron mass, $Z_{\text{eff}} = (1/n_e) \sum_i n_i Z_i^2$ is the effective ion charge for collisions summed over ion species i , e is the electron charge, c is the speed of light, k_B is the Boltzmann constant, T_e is the electron temperature, and $\ln \Lambda_{\text{IB}}$ is the Coulomb logarithm for IB [16]. In conventional units,

$$K = 9.74 \times 10^{-17} \frac{n_e^2}{n_{\text{cr}} (1 - n_e/n_{\text{cr}})^{1/2}} \frac{Z_{\text{eff}} \ln \Lambda_{\text{IB}}}{T_e^{3/2}} \text{ cm}^{-1} \quad (4)$$

with densities in cm^{-3} and temperatures in eV.

As described in Johnston, *et al.* [16], the Coulomb logarithm for a high-frequency laser-plasma interaction, when $\omega > \omega_{pe}$, differs from the standard Coulomb log for low-frequency transport [23] by the replacement $v_{te}/\omega_{pe} \rightarrow v_{te}/\omega$ in evaluating the collisional maximum impact parameter. Recent work [17] highlighted the importance of such corrections, among other atomic physics-related corrections, to correctly predict laser absorption via IB in an experiment. (To allow flexible comparison against other community codes and experimental data, in our implementation we keep $\ln \Lambda_{\text{IB}}$ to be a user-specified function.)

Shearer [24] provided a useful specialization of the laser propagation and deposition problem for the case of oblique laser incidence onto a 1-D plasma density gradient, which we take as along the z direction. In this treatment, the laser has a k -vector component both along and perpendicular to the density gradient, $\mathbf{k} = k_0(0, \sin \theta, \cos \theta)$. We will use this as the basis for our 1-D ray-trace model.

The most important consequence of the oblique incidence is that the laser will reflect and reverse propagation when it reaches a maximum depth of penetration where the density reaches

$$n_m = n_{\text{cr}} \cos^2 \theta_0, \quad (5)$$

where θ_0 is the laser incidence angle in vacuum. If the rays reach a reflection point where $n_e > n_m$, the ray is reflected to the opposite z direction and the ray-trace continues in the opposite direction back out of the domain.

Next, in the oblique incidence case, we replace the initial intensity I_{s0} with

$$I_{z0} = I_{s0} \cos \theta_0, \quad (6)$$

to account for the projected intensity on-target. Finally, we change variables from the propagation direction s to

the target normal z , which gives [24]

$$\frac{dI_z}{dz} = -K_z I_z = -K_0 \frac{n_e^2}{n_{cr} \cos \theta_0} \frac{1}{(1 - n_e/n_m)^{1/2}} I_z. \quad (7)$$

This gives the evolution of the laser intensity and power deposited along the target normal direction z .

This model for laser power deposition into a plasma is convenient because it can be directly integrated in 1-D, which, for specified laser parameters, plasma density, and temperature, gives

$$I_z(z') = I_{z0} \exp\left(-\int_{z_0}^{z'} K_z dz\right), \quad (8)$$

where z_0 is the position from which the rays are launched.

After obtaining $I_z(z')$, the power deposited is found from conservation of energy,

$$P_{abs}(z') = -\frac{dI_z(z')}{dz}. \quad (9)$$

In the case of reflection, the power deposited is summed over the in-going and out-going rays.

This model provides a direct prescription of laser deposition to run in-line in a simulation. At each grid point, the simulation provides the plasma density and temperature input needed to determine K_z . The model can be run in higher-dimensions (i.e., 2-D or 3-D); for example, in the case where the laser intensity has a profile as a function of transverse position, as in $I_0 = I_0(x, y)$. In this case, the solution requires a simple loop over separate z ray-traces for each (x, y) . A time-profile of the laser intensity $I_0 = I_0(t)$ can easily be handled by loading a prescribed initial intensity as a function of simulation time.

We note this model includes the global oblique laser incidence effects, via Eqs. 5–7, but does not include further refraction of the laser in the simulation domain, as is calculated in more complex ray-tracing codes [10]. This limit is valid when the plasma has expanded a distance L_z off the target which is smaller than the laser diameter, so that the plasma still appears nearly 1-D to the approaching laser.

III. NUMERICAL IMPLEMENTATION

A. Integration

To implement the ray-trace model, we integrate Eq. 8 for each ray using laser parameters, spatial plasma density, and temperature information from the simulation to calculate the absorption rate K_z . Trapezoidal quadrature is performed from a specified initial launch point of the rays z_0 through the domain until a point of reflection at the modified critical density or a final specified ray-trace position is reached. If the ray reflects, the ray is traced back along its path out of the plasma. From

energy conservation, the power deposited into the cell is then determined from

$$P_{abs} = -\frac{\Delta I_z}{\Delta z}, \quad (10)$$

where Δz is the grid spacing. The power deposited along the inward propagating and reflected rays are summed to give a total power deposited at each spatial location along z .

It is straightforward to apply different laser intensities as a function of time, since the ray-trace is done for a given time step of the simulation. Secondly, when the simulation is run in higher-dimensions, the user can prescribe a transverse intensity profile for the laser $I_0(x, y)$, and separate ray traces are done along z for each transverse ray position. The final result is the power deposited $P_{abs}(x, y, z, t)$ through the domain at the timestep t , plus auxiliary diagnostic data such as the cumulative K_z integral (optical depth) along the ingoing and outgoing rays.

B. Analytical calculation at the point of reflection

At the maximum density of penetration (n_m), there is a singularity in Eq. 8 that prevents us from using simple numerical quadrature. The singularity is physically related to the reflection of the laser light. However, the actual energy deposited is integrable, so to obtain an accurate solution for the power deposited near this point, the following is performed. First, the trapezoidal quadrature is stopped at the grid point immediately before the point of reflection, which we denote z_r . Second, an analytical calculation is made for ray-trace and power-deposited between z_r and the physical maximum distance of penetration z_m , defined by $n_e(z_m) = n_m$, which may not lie exactly on one of our discrete spatial grid points. Finally, the numerical integration is continued outward, starting again from z_r .

The intensity of the ingoing laser at z_r , denoted I_- , is

$$I_- = I_0 \exp\left(-\int_{z_0}^{z_r} K_z dz\right) \quad (11)$$

and is first found according to the standard ray-tracing procedure outlined above.

The intensity of the outgoing laser at z_r after reflection, denoted I_+ , is then

$$I_+ = I_- \exp\left(-2 \int_{z_r}^{z_m} K_z dz\right). \quad (12)$$

The absorption between z_r and z_m is important as this region often has a significant amount of power deposited resulting from the growth of the denominator in the integral. The solution to calculate the power deposition in this region is to assume a linear density profile between z_r and z_m and use an analytical solution for the integral

to obtain the power deposited between z_r and z_m . The density gradient is assumed to be linear

$$n_e(z) \approx n_{z_r} + (n_m - n_{z_r}) \frac{z - z_r}{\delta}, \quad (13)$$

where $\delta = z_m - z_r$, and the turning point location z_m is inferred from a linear interpolation between z_r and the next gridpoint. Figure 1 illustrates the geometry near the turning point.

The analytical solution for $\int_{z_r}^{z_m} K_z dz$ using a linear density gradient is then

$$\int_{z_r}^{z_m} K_z dz = \frac{2}{15} \frac{\delta K_0}{\cos \theta} \frac{(8n_m^2 + 4n_m n_{z_r} + 3n_{z_r}^2)}{n_{\text{cr}}(1 - n_{z_r}/n_m)^{1/2}} \quad (14)$$

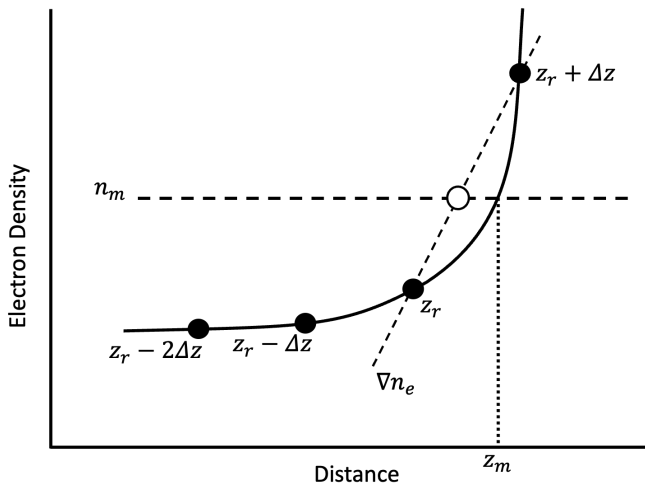


FIG. 1. Analytical linear approximation near the turning point. In this example, z_m is not on our spatial grid, z_r is on the spatial grid, and Δz is the distance between spatial grid points. n_m is known. The density at the black points is known since they fall on our spatial grid. The location of z_m is unknown and approximated linearly, as depicted by the white point.

The additional power deposited at the turning point is, accordingly,

$$\Delta P_{\text{abs}}(z_r) = \frac{I_- - I_+}{\Delta z}. \quad (15)$$

C. Particle Heating

From the above development, we have the power deposited per unit volume at all points along the path of the laser. Within a particle-in-cell code, each macroparticle represents a weighted contribution to the total electron density n_e . Dividing $P_{\text{abs}}(x, y, z)$ by the local density $n_e(x, y, z)$ gives the power deposited by the laser per electron. The heating module then performs a randomized kick to each macroparticle in the associated cell

such that the particle's energy will increase on average by

$$H(x, y, z) = \frac{P_{\text{abs}}(x, y, z)}{n_e(x, y, z)} \Delta t_{\text{heating}}, \quad (16)$$

where H is the energy deposited per electron, and $\Delta t_{\text{heating}}$ is the time-step between calls to the heating module. Per the standard IB theory, given that $m_e \ll m_i$, the heating is applied only to the electrons, which subsequently can heat the ions via standard Coulomb collisions. The energy is distributed to the electrons in a statistical manner by giving each particle an independent randomized momentum kick defined by

$$\Delta \mathbf{p} = \sqrt{\frac{2}{3} m_e H} (r_1 \hat{\mathbf{x}} + r_2 \hat{\mathbf{y}} + r_3 \hat{\mathbf{z}}), \quad (17)$$

where the numbers r_1 , r_2 , and r_3 are randomly sampled from a standard normal distribution. The average energy change per particle is then given by

$$\begin{aligned} \langle \Delta \epsilon \rangle &= \langle (\mathbf{p} + \Delta \mathbf{p})^2 / 2m_e - \mathbf{p}^2 / 2m_e \rangle \\ &= \langle 2(\mathbf{p} \cdot \Delta \mathbf{p}) \rangle / 2m_e + \langle \Delta \mathbf{p}^2 \rangle / 2m_e. \end{aligned} \quad (18)$$

Assuming a well-sampled distribution of particles and small-amplitude kicks uncorrelated to the particle momenta, $\langle (\mathbf{p} \cdot \Delta \mathbf{p}) \rangle \approx 0$, and the chosen amplitude, leads to the desired average energy change per particle

$$\langle \Delta \epsilon \rangle \approx (2/3) m_e H (\langle r_1^2 \rangle + \langle r_2^2 \rangle + \langle r_3^2 \rangle) / 2m_e = H. \quad (19)$$

We note that for the time being, we have implemented the simplest possible kicking mechanism, which is to heat the plasma via Gaussian kicks, drawn from a uniform distribution for all particles. However, more advanced Langevin schemes have been developed that kick the particles in a fashion relevant to IB heating [25], which predominantly heats the coldest particles in the distribution, leading to super-Gaussian particle distributions and the well-known Langdon effect [26]. Implementing such advanced kicking schemes will be pursued in future implementations.

IV. RESULTS AND BENCHMARKS

In this section, we verify the ray-tracing module via several benchmarks. First, we verify that the code and quadrature scheme obtains the expected absorption for analytic plasma profiles, and second, that the scheme conserves energy between the input laser energy and changes to the plasma energy. Finally, we cross-benchmark the ray trace module against a 2-D ray-tracing calculation in the radiation hydrodynamics code FLASH, which includes in-plane laser refraction, and thereby validates how our reduced 1-D model treats oblique incidence. Two separate papers show additional dynamic benchmarking with ablation of a plasma slab

and comparison to various radiation hydrodynamics simulations, verifying along the way that the laser deposition is well-matched between the simulations [21, 22].

Figures 2 and 3 utilize simple electron density profiles (n_e) to benchmark the validity of the 1-D ray trace and numerical integration. These benchmarks test the numerical ray trace for a static plasma. The electron density profiles used for Figs. 2a and 3a are analytically solvable to provide the laser intensity at each spatial location along the path of the laser.

The first benchmark for our laser-energy deposition model is the case of a constant-density plasma with a sub-critical density under the maximum density of penetration ($n_e < n_m$). At a density under n_m , the laser propagates through the plasma without reflection. In this constant density case, the analytical solution for the intensity of the laser is

$$I(z') = I_0 \exp\left(-\frac{K_0}{n_{cr} \cos \theta_0} \frac{n_e^2}{(1 - n_e/n_m)^{1/2}} (z' - z_0)\right), \quad (20)$$

where n_e is a constant and $(z' - z_0)$ is the distance of laser propagation.

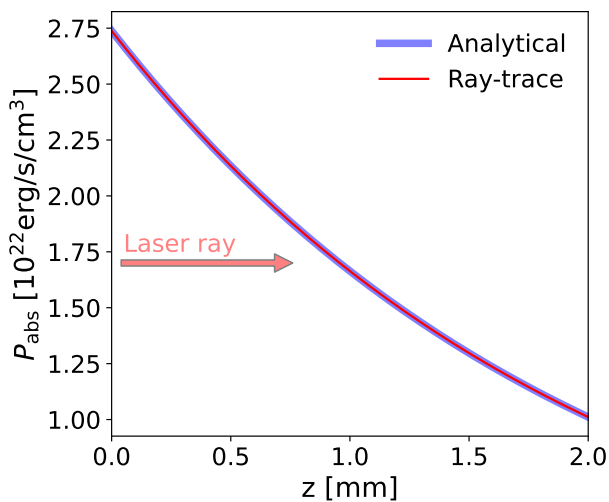


FIG. 2. Analytical and numerical laser power deposition P_{abs} for a constant density profile. The laser at wavelength 351 nm, with intensity 5.5×10^{21} erg/cm²/s, enters from the left and propagates towards the right. The laser is normally incident ($\cos \theta_0 = 1$) onto the uniform plasma with an electron density of 10^{21} cm⁻³, effective charge state $Z_{eff} = 5.29$, and electron temperature of 1800 eV. The results of the numerical and analytical solutions are identical.

Figure 2, shows the result from the numerical raytrace calculation matches exactly with that of the analytical solution. The laser, at wavelength 351 nm with intensity 5.5×10^{21} erg/cm²/s, enters from the left and propagates towards the right. For this laser wavelength, the critical density (n_{cr}) is 9.0496×10^{21} cm⁻³. The laser is normally incident ($\cos \theta_0 = 1$) onto the uniform plasma of

electron density of 10^{21} cm⁻³ $\approx 0.11 n_{cr}$, effective charge state $Z_{eff} = 5.29$, and electron temperature of 1800 eV. The figure shows excellent agreement between the ray-trace model and analytical calculation.

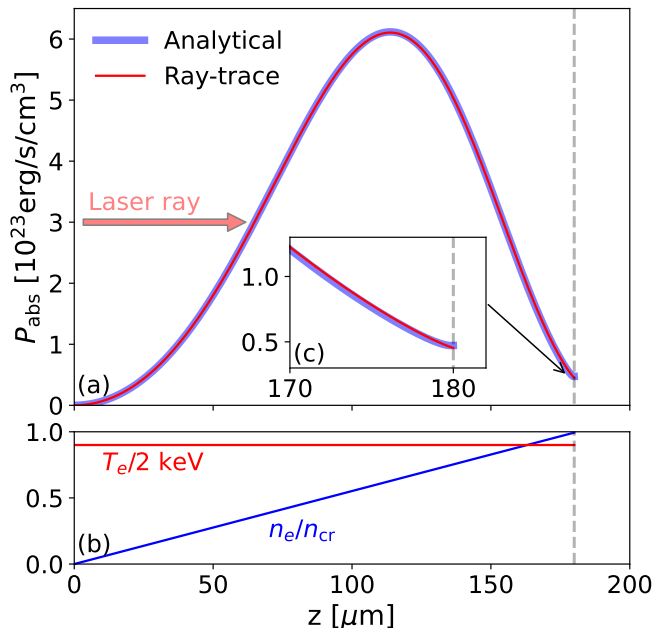


FIG. 3. (a) Laser power absorption in a linear electron density profile calculated analytically (blue) and with the ray-trace model (red). The laser enters from the left and propagates towards the right at normal incidence. (b) Electron density and temperature profiles. (c) A close-up view near the point of reflection where our analytical technique is used for the numerical solution. The point of reflection is shown by the vertical dashed line.

A second benchmark is a linear electron density profile with a peak density higher than n_m , which was originally calculated analytically in Ref. [24]. This benchmark has the benefit of testing the calculation at and near the point of reflection as well as benchmarking the backward propagating ray after reflection. In the case of a linear density gradient, the density profile follows

$$n_e = n_0 \frac{z}{L}. \quad (21)$$

For the test shown in Fig. 3, we use $n_0 = 10^{22}$ cm⁻³, $L = 200$ μ m, and the same laser parameters as for the constant density case. The critical density is again $\approx 9 \times 10^{21}$ cm⁻³, which is reached at $z_m \approx 180$ μ m. The analytical and numerical solutions are shown to be in overall excellent agreement.

As the next benchmarking test, we confirm the overall energy conservation between laser energy input and plasma heat by simulating the irradiation of a uniform electron-ion plasma and comparing the change in the total energy of the plasma with the expected laser absorption. For this test, we assume $T_e = T_i = 10$ eV and

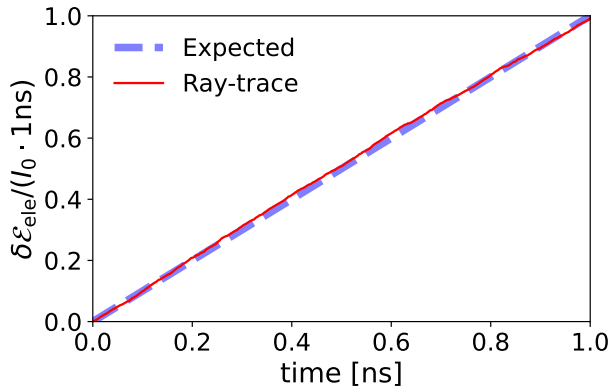


FIG. 4. Temporal evolution of the internal energy areal density gain of the simulated electrons, $\delta\mathcal{E}_{\text{ele}}$ (red solid line), compared to the theoretical prediction for full absorption of a laser with intensity $I_0 = 8 \times 10^{16}$ erg/cm²/s, $I_0 t$ (blue dashed line).

$n_e = 10^{20}$ cm⁻³ for the plasma, $\lambda = 1.064$ μm for the laser wavelength, and $I_0 = 8 \times 10^{16}$ erg/cm²/s for the laser intensity. The one-dimensional simulation domain has a length of ≈ 10 mm and is resolved by a spatial grid with 2000 grid cells and 100 particles per cell for each plasma species. The simulation is run for ≈ 63000 timesteps, corresponding to a total duration of 1 ns. The particle boundaries are reflecting, and the electromagnetic field solver is turned off to isolate the energy change from the laser module. For these parameters, the laser is fully absorbed (to machine precision) approximately midway through the simulation domain, penetrating slightly deeper into the plasma with time as the electron temperature increases and the absorption decreases near the laser input boundary of the domain. Figure 4 shows the temporal evolution of the total energy of the simulated electrons calculated every 100 timesteps (red), which is seen to be in close agreement with the theoretical prediction for full absorption of the laser (dashed line).

Finally, we cross-benchmarked the present laser-ray trace module against the FLASH radiation hydrodynamics code [11]. Notably, the FLASH simulations used a 2-D domain, where a propagating laser can refract within the simulation plane. This allows us to test the present 1-D model, with the oblique incidence corrections of Eqs. 5-7, against a more fundamental model. (Additional benchmarking, including the cross-benchmarking of the subsequent dynamical evolution against FLASH, is described in detail in a companion manuscript [21].) The setup of the test is as follows. We started with the LaserSlab test problem provided with the FLASH distribution [27]. We conducted 2-D FLASH simulations of laser ablation of a solid aluminum slab with initial density of 2.7 g/cm³ and a 50 μm thickness by a laser pulse of 0.3 ns duration with a 0.1 ns linear rise to a flat-top peak intensity of 3.54×10^{11} W/cm², 1 μm wavelength, and a uniform

transverse profile. One of the simulations had normal incidence ($\theta_0 = 0^\circ$) and another used oblique incidence ($\theta_0 = 45^\circ$). The simulation box was 400 by 400 microns, divided into 2×2 blocks containing 16×16 cells each, with a maximum level of adaptive mesh refinement set to 7. We simulated the plasma evolution up to 0.3 ns and then took a cut along the target normal to obtain 1-D profiles for both cases. Then, we conducted two short 1-D PSC simulations initialized directly from these FLASH profiles, running a small number of steps until the first call to the laser ray-trace and deposition module. We adopted a Coulomb logarithm in PSC that identically matched the default version in FLASH. Figure 5 compares PSC and FLASH in terms of the electron density (a,b), temperature (c,d), and laser power deposition (e,f) profiles for normal incidence (a,c,e) and oblique incidence (b,d,f) cases. Note that while the density can be directly loaded into PSC, the temperature will obtain statistical fluctuations due to the finite number of computational particles (Fig. 5c,d). Nevertheless, for these matched density and temperature profiles, the resulting laser absorption profiles are in excellent agreement, as shown in Fig. 5e,f. Insets in Figs. 5a,b depict a zoom-in onto the laser ray reflection region. In the normal incidence case, we see that both FLASH and PSC capture the critical surface location, z_r , observable as the location where the laser absorption profile reaches a maximum and then cuts off in Fig. 5e. In the oblique incidence case, we see that both FLASH and PSC capture an identical maximum penetration depth z_m , now given by $n_e(z_m) = n_m = n_{\text{cr}} \cos^2 \theta_0$. The agreement between the full ray-tracing approach utilized in FLASH and our model using the oblique incidence effects of Ref. [24] demonstrates that this model is effective for capturing the global oblique incidence effects on laser absorption in realistic scenarios.

V. IMPLEMENTATION NOTES

The ray-trace routine was implemented as a separate module in PSC. The present version allows transverse laser intensity profiles, with the restriction that the ray-tracing itself is along one coordinate axis. In this case, a bundle of rays is ray-traced, with one ray per transverse cell in x and y , with each ray's initial intensity set by the intensity profile $I_0(x, y)$.

PSC is implemented using MPI with domain decomposition, where each processor holds the electromagnetic fields and particles associated with particular spatial tiles of the global domain [20]. Periodically, the particle data is used to calculate the moments (density, flows, and temperatures), again held on each processor, which is used for both output and now the ray-trace model.

The ray-trace requires a spatial integral over large volumes of the domain, much larger than the subdomain assigned to each processor. In the present version, the relevant moment data (density n_e , electron temperature T_e), needed for calculating the terms in Eq. 2, are gathered to

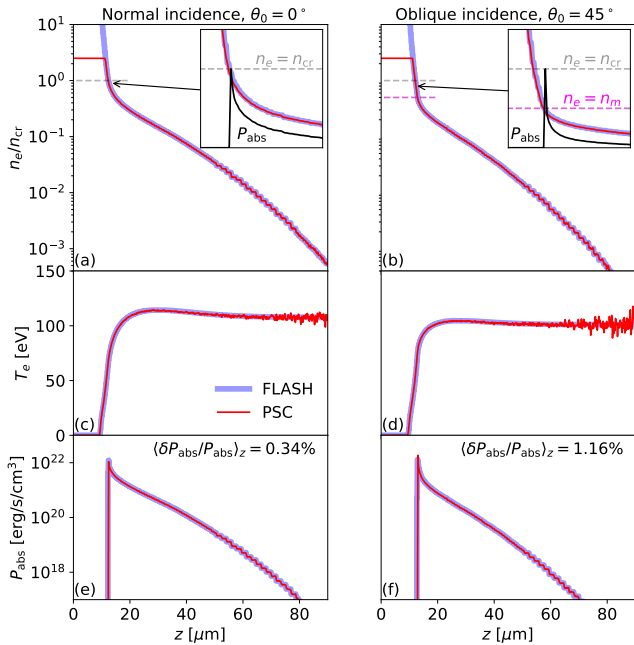


FIG. 5. Testing laser ray tracing and laser energy deposition module in PSC against the FLASH code. (a,b) Electron density, (c,d) temperature, and (e,f) laser power absorption for (a,c,e) normal and (b,d,f) oblique incidence cases. Insets in (a) and (b) depict the zoom-ins around z_r and z_m , respectively. Very good agreement between PSC and FLASH simulations is seen.

one processor (via `MPI_reduce`), which then performs the ray-trace and calculates the laser-energy deposition. The laser-energy deposition information is then distributed back to the full set of processors (via `MPI_scatter`), after which each processor kicks the particles in its own subdomain.

We found that the global data gather could be memory-restrictive for large 2-D simulations. A first optimization, which we have implemented, is to restrict the ray-tracing to a finite subdomain, which limits the memory and communication requirements. This is appropriate when considering plasma ablation from solid targets, where much of the domain can remain at very low density

and therefore negligible absorption. A second optimization, planned for the future, will be to parallelize the ray-trace using several stripes oriented along the ray-tracing direction with a larger set of ray-tracing processors; such a data subdivision is facilitated by the fact that the ray-tracing is only along z .

We found the ray-trace and particle kicks can be significantly sub-cycled compared to the PIC time-step, since the ray-trace will only yield different results after characteristic dynamic times ($\sim L/V$), where L is the system size and V is a typical plasma velocity, whereas the PIC timestep is required to be on the order of the plasma frequency, $\sim \omega_{pe}^{-1}$, with $\omega_{pe}L/V \gg 1$. Sub-cycling is important because the ray-tracing requires a global communication. Furthermore, the ray-trace also requires a recent calculation of the particle moments (density, temperature), which requires a computationally-expensive iteration over the full particle array (by each processor); however, the moments are usually already available since they are periodically calculated for simulation output. Second, the particle kicks can also be sub-cycled as long as $H/T_e \ll 1$, where H is the magnitude of the kick given to the particles; this is useful because again the particle kick step requires an iteration through the full particle array.

VI. DISCUSSION AND CONCLUSIONS

The present paper describes a ray-tracing model for laser-energy deposition, which has been implemented inline in a plasma particle-in-cell code. This will allow kinetic simulation of laser-solid interaction and the physics of ablated plasmas for high-energy-density physics and laboratory plasma astrophysics experiments [3–7]. The model uses a reduced 1-D ray-trace that, however, includes oblique incidence effects, which are important for modifying plasma absorption. The model was benchmarked against analytic solutions and against a 2-D laser ray-tracing code with excellent agreement. Separate papers have presented additional dynamic benchmarking of the laser ray-trace module against plasma evolution in radiation hydrodynamics simulations and have begun to show the kinetic plasma physics, which can now be studied with this multi-physics capability [21, 22].

[1] H. G. Rinderknecht, P. A. Amendt, S. C. Wilks, and G. Collins, Kinetic physics in ICF: present understanding and future directions, *Plasma Phys. Contr. Fus.* **60**, 064001 (2018).
 [2] C. N. Danson, C. Haefner, J. Bromage, T. Butcher, J.-C. F. Chanteloup, E. A. Chowdhury, A. Galvanauskas, L. A. Gizzi, J. Hein, D. I. Hillier, and et al., Petawatt and exawatt class lasers worldwide, *High Power Laser Sci. Eng.* **7**, e54 (2019).

[3] W. Fox, J. Matteucci, C. Moissard, D. B. Schaeffer, A. Bhattacharjee, K. Germaschewski, and S. X. Hu, Kinetic simulation of magnetic field generation and collisionless shock formation in expanding laboratory plasmas, *Phys. Plasmas* **25**, 102106 (2018).
 [4] D. B. Schaeffer, W. Fox, J. Matteucci, K. V. Lezhnin, A. Bhattacharjee, and K. Germaschewski, Kinetic simulations of piston-driven collisionless shock formation in magnetized laboratory plasmas, *Physics of Plasmas* **27**, 10.1063/1.5123229 (2020).

- [5] K. V. Lezhnin, W. Fox, D. B. Schaeffer, A. Spitkovsky, J. Matteucci, A. Bhattacharjee, and K. Germaschewski, Kinetic simulations of electron pre-energization by magnetized collisionless shocks in expanding laboratory plasmas, *Astrophys. J. Lett.* **908**, L52 (2021).
- [6] W. Fox, G. Fiksel, A. Bhattacharjee, P.-Y. Chang, K. Germaschewski, S. X. Hu, and P. M. Nilson, Filamentation instability of counterstreaming laser-driven plasmas, *Phys. Rev. Lett.* **111**, 225002 (2013).
- [7] W. Fox, A. Bhattacharjee, and K. Germaschewski, Fast magnetic reconnection in laser-produced plasma bubbles, *Phys. Rev. Lett.* **106**, 215003 (2011).
- [8] J. Matteucci, W. Fox, A. Bhattacharjee, D. B. Schaeffer, C. Moissard, K. Germaschewski, G. Fiksel, and S. X. Hu, Biermann-battery-mediated magnetic reconnection in 3d colliding plasmas, *Phys. Rev. Lett.* **121**, 095001 (2018).
- [9] J. M. Dawson, On the Production of Plasma by Giant Pulse Lasers, *Phys. Fluids* **7**, 981 (1964).
- [10] T. B. Kaiser, Laser ray tracing and power deposition on an unstructured three-dimensional grid, *Phys. Rev. E* **61**, 895–905 (2000).
- [11] P. Tzeferacos, M. Fatenejad, N. Flocke, C. Graziani, G. Gregori, D. Lamb, D. Lee, J. Meinecke, A. Scopatz, and K. Weide, FLASH MHD simulations of experiments that study shock-generated magnetic fields, *High Energy Dens. Phys.* **17**, 24 (2015).
- [12] C. Thoma, D. R. Welch, R. E. Clark, D. V. Rose, and I. E. Golovkin, Hybrid-pic modeling of laser-plasma interactions and hot electron generation in gold hohlraum walls, *Phys. Plasmas* **24**, 062707 (2017).
- [13] M. M. Basko and I. P. Tsygvintsev, A hybrid model of laser energy deposition for multi-dimensional simulations of plasmas and metals, *Comp. Phys. Comm.* **214**, 59 (2017).
- [14] T. D. Arber, K. Bennett, C. S. Brady, A. Lawrence-Douglas, M. G. Ramsay, N. J. Sircombe, P. Gillies, R. G. Evans, H. Schmitz, A. R. Bell, and C. P. Ridgers, Contemporary particle-in-cell approach to laser-plasma modelling, *Plasma Phys. Control. Fus.* **57**, 113001 (2015).
- [15] Y. Zhang, F. Wang, J. Liu, and J. Sun, Simulation of the inverse bremsstrahlung absorption by plasma plume in laser penetration welding, *Chem. Phys. Lett.* **793**, 139434 (2022).
- [16] T. W. Johnston and J. M. Dawson, Correct values for high-frequency power absorption by inverse bremsstrahlung in plasmas, *Phys. Fluids* **16**, 722–722 (1973).
- [17] D. Turnbull, J. Katz, M. Sherlock, L. Divol, N. R. Shaffer, D. J. Strozzi, A. Colaitis, D. H. Edgell, R. K. Follett, K. R. McMillen, P. Michel, A. L. Milder, and D. H. Froula, Inverse bremsstrahlung absorption, *Phys. Rev. Lett.* **130**, 145103 (2023).
- [18] T. Takizuka and H. Abe, A binary collision model for plasma simulation with a particle code, *J. Comp. Phys.* **25**, 205 (1977).
- [19] R. Devriendt and O. Poujade, Classical molecular dynamic simulations and modeling of inverse bremsstrahlung heating in low Z weakly coupled plasmas, *Phys. Plasmas* **29**, 073301 (2022).
- [20] K. Germaschewski, W. Fox, S. Abbott, N. Ahmadi, K. Maynard, L. Wang, H. Ruhl, and A. Bhattacharjee, The Plasma Simulation Code: a modern particle-in-cell code with patch-based load-balancing, *J. Comp. Phys.* **318**, 305 (2016).
- [21] K. V. Lezhnin, S. R. Titorica, A. S. Hyder, J. Griff-McMahon, M. B. P. Adams, P. Tzeferacos, A. Diallo, and W. Fox, Particle-in-cell simulations of expanding high energy density plasmas with laser ray tracing (2024), arXiv:2409.17327 [physics.plasm-ph].
- [22] S. R. Titorica, K. Lezhnin, D. J. Hemminga, J. Gonzalez, J. Sheil, A. Diallo, A. Hyder, and W. Fox, Acceleration mechanisms of energetic ion debris in laser-driven tin plasma EUV sources, *Appl. Phys. Lett.* **124**, 174101 (2024).
- [23] J. Huba, *NRL Plasma Formulary* (Naval Research Lab., Washington, DC, 2004).
- [24] J. W. Shearer, Effect of oblique incidence on optical absorption of laser light by a plasma, *Phys. Fluids* **14**, 183 (1971).
- [25] F. Detering, V. Y. Bychenkov, W. Rozmus, R. Sydora, and C. Capjack, Langevin representation of laser heating in PIC simulations, *Comp. Phys. Comm.* **143**, 48 (2002).
- [26] A. B. Langdon, Nonlinear inverse bremsstrahlung and heated-electron distributions, *Phys. Rev. Lett.* **44**, 575 (1980).
- [27] *FLASH User's Guide* (Flash Center for Computational Science, University of Rochester, 2023).